Three-dimensional simulations of reshocked inclined Richtmyer-Meshkov instability: Effects of initial perturbations

Mohammad Mohaghar, Jacob McFarland, and Devesh Ranjan

Phys. Rev. Fluids **7**, 093902 — Published 12 September 2022

DOI: 10.1103/PhysRevFluids.7.093902

Three-dimensional simulations of reshocked inclined Richtmyer-Meshkov instability: effects of initial perturbations

Mohammad Mohaghar,[1,*] Jacob McFarland,[2] and Devesh Ranjan[1]

[1] *George W. Woodruff School of Mechanical Engineering, Georgia Institute of Technology, Atlanta, GA 30332, USA*

[2] *Department of Mechanical Engineering, Texas A&M University, College Station, TX 77843, USA*

(Dated: August 26, 2022)

Abstract

The effect of initial perturbations on the evolution of inclined Richtmyer–Meshkov turbulent mixing layer before and after reshock initiated by a shock wave with Mach number 1.55 is investigated through three-dimensional simulations using the FLASH code. The 3D simulations aims to reproduce both predominantly single-mode and multi-mode interfaces between light and heavy gases (N_2/CO_2, Atwood number, $A \approx 0.22$; amplitude to wavelength ratio of 0.088) which were created in an inclined shock tube facility to analyze the effects of initial conditions on mixing development in the entire flow field. The two-dimensional center slices of 3D simulations are compared with the experimental results to validate the computational code. Mixing width, mixed-mass, mixed-mass thickness and circulation in addition to concentration fields are shown to be in good agreement with the experimental data. The three-dimensional density and vorticity fields are first presented to qualitatively describe the flow behavior before and after reshock. Several measured density/velocity related quantities indicate that the growth of the mixing material is strongly dependent on initial conditions. Before reshock and at early times after reshock, flow is clearly maintaining the memory of initial perturbations. However, at late time after reshock, although the large wavelength feature still dominates the flow motion and the morphology of the two different interfaces indicate several differences, by breakdown of large scale coherent structures to much finer scales, the memory of small scales of the multi-mode initial perturbation is not as clear as pre-reshock. Regarding three-dimensionality of the flow, before reshock in the multi-mode case, the baroclinic vorticity production, circulation, turbulent kinetic energy and turbulent mass-flux suggest that the small scale roll-up features along the large inclined wavelength quickly evolves in all three dimensions. The coherent vortex tubes break down to smaller worm-like vortex structures and turbulent fluctuations in the out-of-plane dimension is comparable to the spanwise direction. After reshock, this three-dimensionality of mixing growth was observed in the flow for both initial conditions. The results of this work represent a significant extension of previous computational studies performed on this specific topic. A different code with a different numerical method is validated through comparison with the experimental data. The initial perturbations are directly measured from the experimental results. Moreover, the entire three-dimensional experimental shock tube domain is simulated and more quantities are investigated to understand the mixing mechanism and instability evolution in all three dimensions.

I. INTRODUCTION

The Richtmyer-Meshkov instability (RMI) is a fundamental hydrodynamic instability that occurs when an interface between two materials with different densities is impulsively accelerated [4, 5]. This impulsive acceleration occurs when a shock wave passes through the interface. In RMI, the instability is initiated and evolved by the deposition of vorticity at the interface, which is caused by the misalignment between density and pressure gradients across the interface between materials and impulsive acceleration (shock wave) [6, 7]. This deposited vorticity at the interface stretches the surface area between the two materials and rapidly increases the mixing, which leads to the development of small scale structures along the interface due to Kelvin-Helmholtz instability. Merging of these small scale vortices along the interface can drive the transition to turbulent mixing state. Similar to the Rayleigh-Taylor instability (RTI), the initial growth of interface in the RMI is linear and the instability evolves to nonlinear and turbulent states, however unlike RTI, RMI can be developed regardless of the relative position of the materials at the interface (heavy/light or light/heavy) [8, 9]. Studying RMI is important for several engineering applications such as understanding mixing in inertial confinement fusion [10], astrophysical explosions [11], and supersonic combustion [12].

One of the key ingredients that affect the growth of the mixing region in the RMI is the characteristics of initial perturbations. Several experimental and computational studies aimed to understand the degree to which memory of the initial conditions can be retained at different stages of development of instability and how the initial perturbations can affect the statistics of the flow at late time [13–16]. Several experimental studies recently measured both velocity and density related quantities using simultaneous planar laser-induced fluorescence (PLIF) and particle image velocimetry (PIV) techniques. However, these measurements only provided statistics in a two dimensional plane [1, 2, 17–19]. In addition, there are not any experimental studies so far that provide simultaneous measurements of density and pressure to directly compute baroclinic production term. Therefore, numerical simulations can help to provide a better understanding of the effects of initial conditions on mixing progress in the entire flow field in different stages of RMI development.

Many high resolution simulations have been performed to study effect of initial per-

* mohaghar@gatech.edu

turbations, different geometries and reshock on mixing in the RMI. Thornber *et al.* [20] investigated RMI induced by two different, multi-mode initial conditions using large eddy simulation (LES). Groom and Thornber [21] extended this study by analyzing the effects of varying the bandwidth and spectral exponent of the initial perturbations on RMI development. The effect of reshock was studied by Hill *et al.* [22], where they performed LES using a hybrid shock-capturing scheme in an adaptive mesh refinement (AMR) framework. In addition, Latini *et al.* [23] also studied the effects of reshock on the RMI at late time by utilizing a weighted ninth-order weight essentially nonoscillatory (WENO) shock-capturing method. Morán-López and Schilling [24] have also used WENO flux reconstruction in simulations to study the variable density physics and associated evolution of turbulent kinetic energy in RMI. The LES method was later used to investigate the dependence of Atwood number and Mach number on RMI growth [25, 26]. Tritschler *et al.* [27] quantified the uncertainties of turbulence statistics introduced by the numerical methods. Recently, Wong *et al.* [28] examined the variable-density statistics of the RMI under different Reynolds numbers in addition to investigating the sensitivities of time-dependent statistics on grid resolution for 2D and 3D simulations.

The current computational study is an extension to the previous experimental and computational studies [1–3, 29]. Mohaghar *et al.* [1] performed shock tube experiments between nitrogen (seeded with acetone) and carbon dioxide using two different initial conditions. The first of these was a predominantly single-mode interface, created by inclining the shock tube by 80° relative to the ground, while the second was a multi-mode interface that is created by injecting heavy/light gas above/below the stagnation plane between the two gases, which is inclined at 10° relative to the y-axis/shock as in the single-mode case. In both cases the amplitude to wavelength ratio was 0.088 due to the inclination of shock tube, which lead to the large-scale single mode. McFarland *et al.* [3] studied the modal interactions of the initial conditions using the ARES code, developed at Lawrence Livermore National Laboratory. The study includes an extension to 3D and other improvements upon the work in McFarland *et al.* [30]. The results of the RMI evolution for the single-mode perturbations in these simulations were compared with the results of experiments conducted at the experimental facility of Mohaghar *et al.* [1, 2] and Mohaghar [29]. However, since the multi-mode perturbations in the experiments were conducted after these simulations [3], the initial perturbations in those computational studies were different from the experimental results, and thus the RM development of the multi-mode case could not be compared directly with the experiments. The main differences between this study and the previous computational study of McFarland *et al.* [3] are: 1) The processed experimental PLIF images of initial perturbations [1, 29] are used for the computational setup of multi-mode perturbations to be able to directly compare the computational results with the experimental ones. 2) The entire domain of experimental shock tube is simulated instead of only the center region to understand the interaction between large and small scales and mixing evolution in the entire volume. 3) The computational results are validated by comparing several quantities computed from experimental data and simulation.

The paper is structured as follows. First, details about the computational domain and initial conditions are explained. Then, the center two-dimensional slices are compared with the experimental results to validate the computational work. Finally, the entire flow field and the three-dimensionality of different variables are analyzed through several density and velocity related quantities before and after reshock.

II. NUMERICAL METHOD

FLASH is an open-source hydrodynamics code developed by the FLASH center at the University of Chicago [31]. FLASH is a modular, adaptive, and scalable multiphysics simulation code for compressible flow. Adaptive Mesh Refinement (AMR) techniques are used to cover large dynamic ranges of problem scales. We use the PARAMESH package, incorporated into FLASH, for AMR, providing a block-structured mesh. The resolution is increased for areas of greater interest, by a factor of 2, in each direction, for each level of refinement. FLASH is a conservative hydrodynamics code and requires that fluxes crossing a common zone face split between different AMR levels are conserved.

Hydrodynamics are handled using various solvers including both split and unsplit implementations of the piecewise parabolic method (PPM), used for this work. The PPM can be described as a finite volume method and is nominally 2nd order in time and space, though spatial interpolation of variables is done through a 4th order cubic polynomial. Discontinuities are treated by solving the Riemann shock-tube problem at each zone interface. A contact discontinuity steepening procedure is used to preserve sharp interfaces, and a flattening method is used to prevent spurious oscillations near shock waves. This method interpolates between zones on a Cartesian grid using parabolas instead of linear interpolation schemes in order to better represent smooth spatial gradients. Calder *et al.* [32] described the code including the results of test calculations.

Flash solves the Euler equations in one dimension using the Strange splitting for multi-dimensional simulation [33]. In this method, one-dimensional sweeps are performed in the X, Y, and Z directions, then in the reverse order over two time steps, preserving 2nd order accuracy in time. FLASH has several equations of state (EOS) available, but here the multi-gamma EOS is used. This EOS follows the ideal gas law but allows for multiple species to be tracked and weighted average adiabatic indices used. Species fractions are tracked, but only a single thermodynamic state (e.g. temperature, pressure, energy) exists. As physical viscosity is not included in the equations and no sub-grid model is used, energy is dissipated at the under-resolved scales through implicit numerical dissipation. Thus, FLASH may be categorized as an implicit large eddy simulation (iLES) code.

III. SIMULATION SETUP BASED ON EXPERIMENTAL INITIAL CONDITIONS

The simulation conditions used in this paper were chosen to match the experimental conditions of Mohaghar *et al.* [1]. Both single- and multi-mode cases for this study will consist of an interface with N_2 over CO_2 with an incident shock wave Mach number of 1.55 into atmospheric pressure. The initial perturbation for the single-mode case is set up with an initially diffused layer prescribed by an error function based on experimental measurements with an inclination angle of 10° with respect to y axis. The mass fraction in the diffusion thickness region is defined as

$$m(x) = 0.5(1 - erf[(x - x_i)S_f/\Delta]), \tag{1}$$

where the interface is initially at x_i, the thickness is Δ through the mixture fraction m, and $S_f = 2|erf^{-1}(1 - 2\varepsilon)|$ is a scaling factor that ensures m varies from a threshold value of ε to $1 - \varepsilon$ over a width Δ [34]. The threshold value ε was chosen as 10^{-5}, which yield $S_f \approx 6 \times 10^{-2}$ m. The diffusion thickness of 1.14 cm for the single-mode case was chosen based on the PLIF images of the experimental interface, which was computed as a 5%–95% species mass fraction. This implies that the computational profile goes from 0.99999 to

0.00001 over the same distance that the experimental profile goes from 0.95 to 0.05. Since the experimental results of Mohaghar [29] suggested that the interface in the third dimension is not perfectly flat in the $x-z$ plane, a cosine function with a small amplitude of 0.2 cm is defined for the $x-z$ plane. For the multi-mode initial condition, two different sets of 10 corrected PLIF images were ensemble-averaged. Then, the location of the interface between the two fluids was extracted using the gradient-based Canny edge detection method. The chosen concentration threshold value was 0.3. For the $x-z$ plane, the ensemble-averaged images were rotated by 10° to be parallel to the y axis. The interface edge of these ensemble averaged images are shown in Fig. 1. The best fit of a combination of sinusoidal functions to the detected interfaces was computed and used as the initial condition of the multi-mode interface in the simulation. The equation of the interface in the $x-y$ and $x-z$ planes defined as

$$x(y, z) = a_{1i} sin(b_{1i} y + c_{1i}) + a_{2i} sin(b_{2i} z + c_{2i}), \tag{2}$$

where the computed coefficients are presented in Table I. The number of sinusoidal modes of the fitted lines (8 for $x-y$ plane and 7 for $y-z$ plane) is computed based on the error between the edge detected points and the fitted line to be less than 5%. The diffusion thickness of the multi-mode interface was defined as 1.84 cm based on the ensemble average of diffusion thickness for 200 corrected PLIF images. It should be noted that since the previous computational work by McFarland *et al.* [3] was performed before the experimental work [1], the diffusion thickness in that work was around 5 cm, which was much higher than the experimental diffusion thickness and the equation of the interface was not similar to the experimental one. Thus, the multi-mode results of the previous computational work by McFarland *et al.* [3] could not be validated by comparing with the experimental results.

In order to simulate the shock tube environment, the computational domain was 11.43 cm in the y direction (spanwise), 11.43 cm in the z direction (out-of-plane) and 175 cm in the x direction (streamwise). The left wall on the x direction was setup to have an outflow boundary condition so as to maintain the constant strength of the shock wave. All the other walls were made fully reflecting. The shock wave and interface were initialized at locations similar to the experimental shock tube, where the interface was 1.6 m above the bottom wall. The computational domain for the 3D simulations of single- and multi-mode initial perturbations is shown in Fig. 2. A summary of gas properties is given in Table II. The

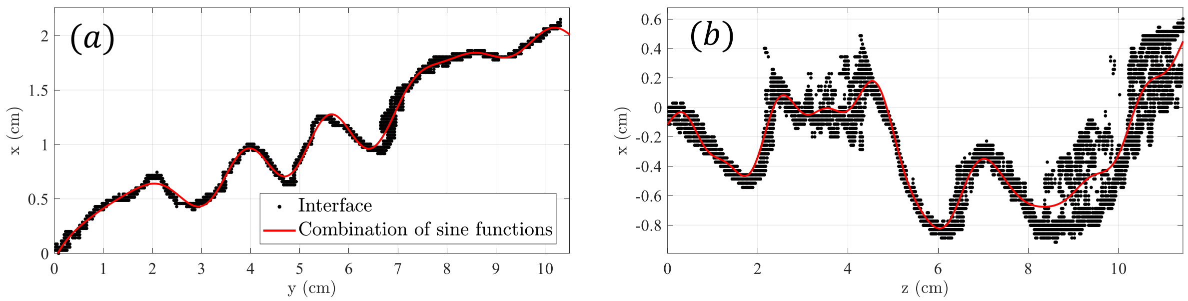

FIG. 1: The interface edge of ensemble average of ten multi-mode initial condition PLIF images and a sinusoidal function fit to the detected interface. Two separate ensemble average images were used for (a) $x-y$ and (b) $x-z$ planes of multi-mode initial condition of 3D simulation. The images were rotated by 10° for $x-z$ plane.

TABLE I: Coefficients of the sine functions for the multi-mode initial perturbation.

i	a_{1i}, a_{2i}	b_{1i}, b_{2i}	c_{1i}, c_{2i}
1	0.3574,0.4606	0.2917,0.2949	-1.007,-3.471
2	2.702,0.1876	0.5181,1.549	0.7046,2.332
3	0.1371,0.2924	2.96,0.8371	3.182,-1.879
4	1.071,3.88	0.8048,2.619	1.938,-1.007
5	0.1019,1.757	3.738,2.72	-0.3787,1.555
6	0.2494,2.375	1.284,2.55	2.337,-3.769
7	0.06439,0.0485	2.47,5.484	1.921,1.053
8	0.03828,0	4.349,0	2.515,0

initial Atwood number pre-shock, $A = (\rho_{CO_2} - \rho_{N_2})/(\rho_{CO_2} + \rho_{N_2})$, across the interface is 0.22.

IV. GRID SENSITIVITY ANALYSIS

The grid sensitivity is analyzed to investigate the sensitivity of different numerical results to the grid spacing. Different grids that are used for this study are summarized in Table III. The first two grids (D and E) are started from 2 levels of mesh refinement as a base resolution and goes up to the maximum of 4 and 5 levels of adaptive mesh refinement (AMR) levels.

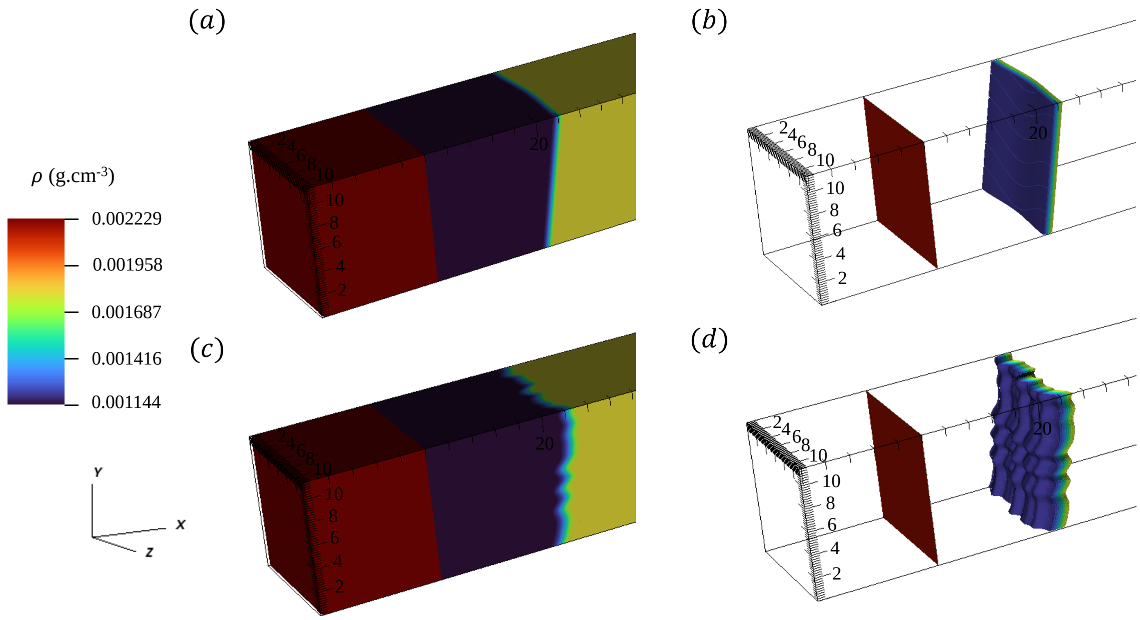

FIG. 2: Illustration of the shock tube test section having a square cross-sectional width of 11.43 cm considered in the computational domain, showing initialization of the interface, shock wave and coordinate system for (a,b) pre-dominantly single-mode interface, and (c,d) multi-mode interface.

TABLE II: Initial conditions of the preshock, postshock and post reshock states of the light- and heavy-fluid sides. i is after incident shock, r indicates after reshock and t is an indicator of transmitted shock. 1 and 2 indicate light and heavy gases respectively.

M_i	M_t	M_r	ρ_1 (kg/m^3)	ρ_2 (kg/m^3)	ρ_1^i (kg/m^3)	ρ_2^i (kg/m^3)	ρ_1^r	ρ_2^r	T_1^i (K)	T_2^i (K)	T_1^r (K)	T_2^r (K)	A	A^i	A^r
1.55	1.61	1.53	1.16	1.84	2.45	3.97	4.39	7.37	403	386	510	471	0.22	0.23	0.25

The base level of mesh refinement are increased to 3 for grids F and G, and the maximum mesh refinement levels are also increased to 6 and 7, respectively. The finest grid spacing for the maximum resolution (maximum refinement level of 7) is 223.2 μm, which is higher than the PIV resolution of 372 μm/vector spacing for high-resolution experimental results [1], and the lowest maximum level of refinement of 4 (the finest grid spacing of $\approx$ 1.8 mm) is chosen to be close to the resolution of high-speed experimental campaign [35].

The grid sensitivities of mixing width (h), integrated turbulent kinetic energy (TKE), and integrated enstrophy (Ω) are analyzed by investigating the differences between the temporal evolution of these quantities for each grid. The mixing width is a length scale

Grid	Base grid resolution	Min refinement level	Max refinement level	Finest grid spacing (μm)
D	$240 \times 16 \times 16$	2	4	1785.6
E	$240 \times 16 \times 16$	2	5	892.8
F	$480 \times 32 \times 32$	3	6	446.4
G	$480 \times 32 \times 32$	3	7	223.2

TABLE III: Different grids used for the 3D simulation. The base resolution is based on the minimum mesh refinement level times the initial number of blocks for each direction.

that approximates the temporal evolution of large-scale features of the instability, which is defined as the 5%–95% extent (in the shock propagation direction) of spanwise-averaged nitrogen volume fraction [36]. The amount of tubulent kinetic energy (TKE) and enstrophy created by incident shock and reshock are calculated as

$$TKE = \int \frac{1}{2}\rho u_i'' u_i'' dV, \tag{3}$$

$$\Omega = \int \frac{1}{2}\rho\omega \cdot \omega, \tag{4}$$

where $\omega = \nabla \times v$, and the velocity fluctuation, u_i'', is calculated using $u_i'' = u_i - \tilde{u}_i$. The Favre (density-weighted) average of velocity is computed using $\tilde{u}_i = \overline{\rho u_i}/\overline{\rho}$.

Although there is not any transport across the walls, the integral and averaged quantities in this study are computed 0.5 cm further from the side walls to remove any wall effects in all analysis. This means that the entire size of the volume that is used for all quantitative analysis is 10.43 cm×10.43 cm×175 cm. Figure 3 shows the temporal evolution of above-mentioned quantities for both single- and multi-mode cases computed using different grids. The growth of mixing width for both single- and multi-mode cases is shown in Figs. 3a and 3b. This quantity is mainly dominated by the large-scale features of the flow, and the large shear effect in the inclined interface is the main cause of the entrainment of the fluids during the RMI evolution. By comparing the results of mixing width for different grids, it can be observed that Grid convergence is obtained at the highest resolution.

Figures 3c and 3d show the grid sensitivity analysis for Turbulent kinetic energy (TKE). In this inclined perturbed flow configuration, after the initial kinetic energy deposition due

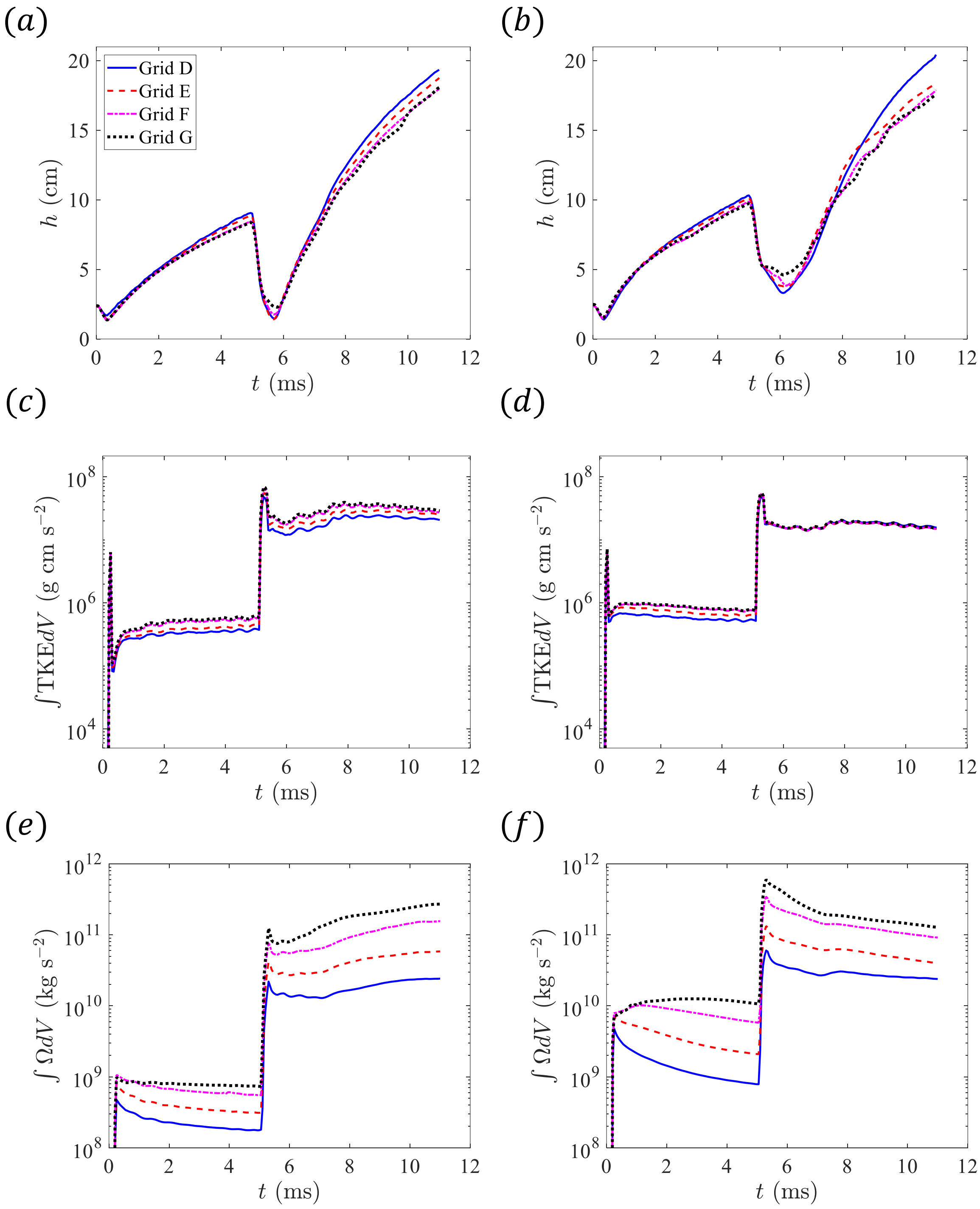

FIG. 3: Grid sensitivities of different statistical quantities over time: (a,b) mixing width, (c,d) integrated turbulent kinetic energy, and (e,f) integrated enstrophy for (a,c,e) single-mode and (b,d,f) multi-mode cases.

to the shock and reshock passages, kinetic energy is largely affected by the strong shear effect between two fluids. Therefore, the lower wave-number eddies (larger scales) are carrying the larger portions of the kinetic energy in the flow. Similar to mixing width, the TKE is also fully converged at the highest grids of F and G.

In addition, the grid convergence for enstrophy is also analyzed for both initial conditions and is shown in Figs. 3*e* and 3*f*. Tritschler *et al.* [27] and Wong *et al.* [28] observed that grid convergence is stricter for enstrophy compared to TKE and mixing width, since esntrophy is related mainly to the small scale features of the flow close to Kolmogorov and Batchelor scales. Similar to these studies, the grid convergence for enstrophy computed for both singe- and multi-mode cases is only obtained at very early time after incident shock. Although the difference between the enstrohphy computed using different grids is reduced by increasing the mesh refinement level, the simulations are still far from resolving high-wave number features in the flow and DNS level. All analysis that are included in this study in the following sections are computed using the finest grid size (grid G).

V. COMPARISON OF TWO-DIMENSIONAL CENTER SLICES OF THREE-DIMENSIONAL SIMULATIONS TO EXPERIMENTAL RESULTS

The simulation results were first compared with experimental results of Mohaghar *et al.* [1] to verify the accuracy of simulation and to examine the factors that contribute most to the disagreement between experiments and computation. In this process experimental results were compared with 2D center slices of the 3D simulation results. Below a qualitative comparison of the concentration fields in the experimental and computational results will be presented, followed by a quantitative comparison between simulations and experiments using mixing width, mixed-mass and mixed-mass thickness and circulation quantities.

A. Visualization of concentration fields

The processed experimental PLIF images, and the 2D center slices of the N_2 mole fraction (concentration) fields for the single- and multi-mode initial perturbations at two times before reshock and two times after reshock (reshock occurs at $t = 5.05$ ms) are plotted and compared in Figs. 4 and 5, respectively. Although the overall length and position of the

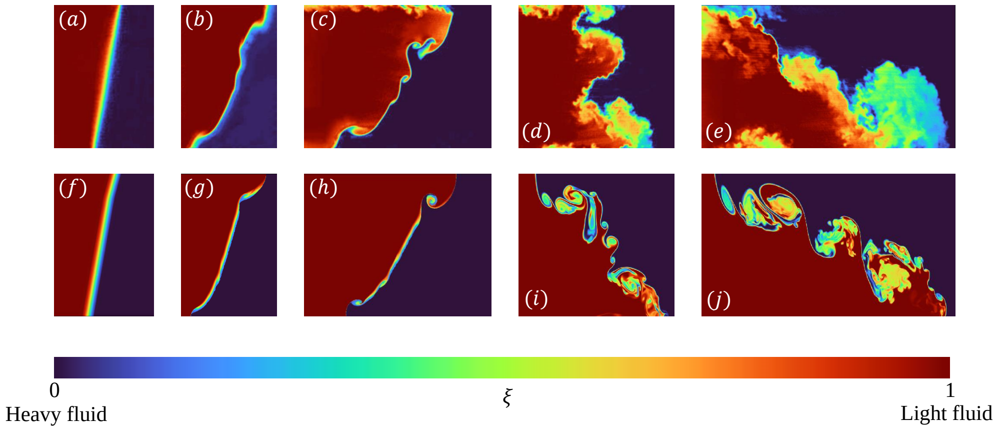

FIG. 4: Concentration fields at different times for pre-dominantly single-mode interface before and after reshock. The concentration fields in the top row (*a*-*e*) are based on the corrected PLIF images of the experimental interface and the bottom row (*f*-*i*) are center slices of N_2 mole fraction fields. The experimental/simulation times are (*a*,*f*) t=0 ms (IC), (*b*,*g*) t=2.64 ms (before reshock), (*c*,*h*) t=5 ms (before reshock), (*d*,*i*) t=6.4 ms (after reshock), (*e*,*j*) t=9 ms (after reshock).

interface, i.e. the large scale features, agree well before and after reshock for both initial conditions, the small scale features exhibit some differences. One immediate observation is that there are more fine-scale structures in the experiment especially in the single-mode case after reshock compared to the simulation results. The development of the roll-up features and their distribution along the interface is very similar to that of the experiment. At early times before reshock, the vortices show similar positions and developments. However, the largest vortex structure in the tip of the bubble just prior to reshock is larger in the experiment compare to the simulation. While the position of vortices and the merging of roll-up features agree well between simulation and experiment, there is a larger accumulation of mass and hence mixing in the experiments. After reshock, the effect of these larger vortex structures are highlighted more clearly in the tip of the bubble and spike regions, where the bubble exhibits more mixed materials compared to the simulation. Part of this mixing in the tip of the bubble and spike regions after reshock is due to the effect of overturning motion, which can cause mixing of the fluid along the interface with the top and bottom boundary layers. Overall, the 2D center slices of the simulation fields agree well with the experimental PLIF images, however there are small differences in the mixed material along the interface,

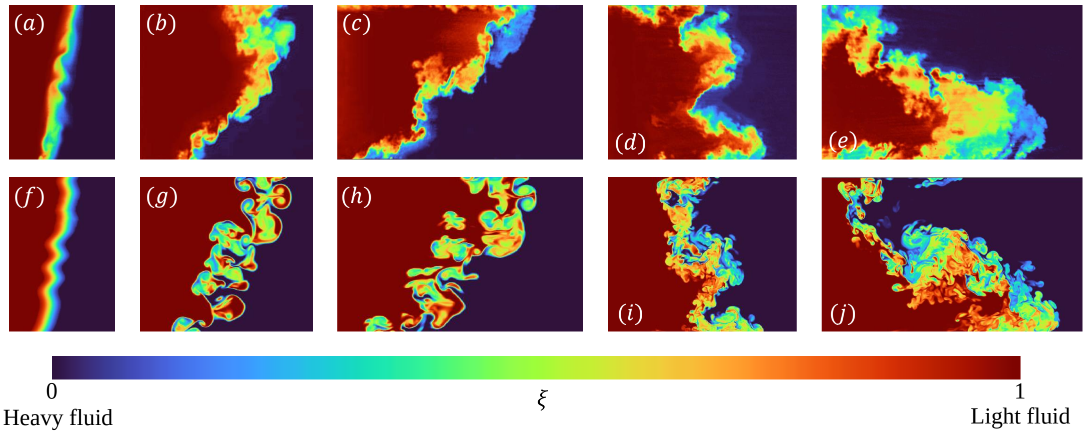

FIG. 5: Concentration fields at different times for multi-mode interface before and after reshock. The concentration fields in the top row (*a*-*e*) are based on the corrected PLIF images of the experimental interface and the bottom row (*f*-*i*) are center slices of N_2 mole fraction fields. The experimental/simulation times are (*a*,*f*) t=0 ms (IC), (*b*,*g*) t=2.64 ms (before reshock), (*c*,*h*) t=5 ms (before reshock), (*d*,*i*) t=6.4 ms (after reshock), (*e*,*j*) t=9 ms (after reshock).

specially in the single-mode case after reshock which can be mainly due to four reasons: 1) The top and bottom boundary layers in the experiments affect mixing before and after reshock. 2) The diffusion thickness may be larger and varies along the out-of-plane dimension in the experiment. 3) The resolution of the simulation is lower than PLIF images of experiments [1]. 4) The effective numerical viscosity is greater than the physical viscosity in the experiment, and thus the numerical diffusion and dissipation which is effectively setting Reynolds number in the simulations may reduce the fine scale mixing.

B. Mixing width, mixed-mass and mixed-mass thickness

The qualitative comparison can be quantified more precisely by considering quantitative measure of the 5%-95% mixing width (h), and the integral measurements of mixed-mass ($\mathcal{M}$) and mixed-mass thickness (δ). The mixing width, which is related to the large-scale features of the instability, is shown in Fig. 6 (a) for both single- and multi-mode cases. The comparison between experimental and simulation results indicates that there is a good agreement between simulation and experiment. This agreement is due to the fact that

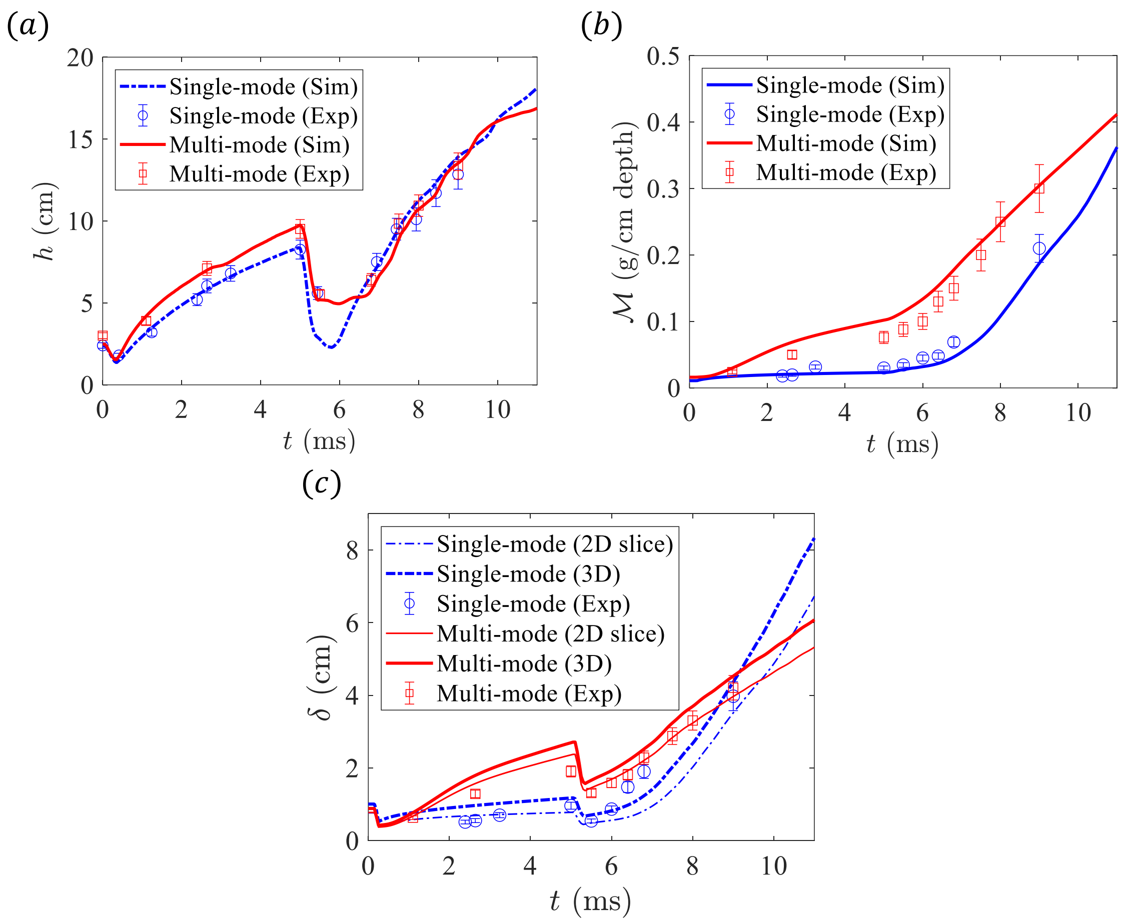

FIG. 6: Comparison of (a) 5%-95% mixing width (h), (b) the integral measurement of mixed-mass $(\mathcal{M})$, and (c) mixed-mass thickness (δ) between the center slices of 3D simulations and experimental results for single- and multi-mode IC.

mixing width is measuring the amplitude, which is the largest scale in the flow. In addition, the single- and multi-mode interfaces, show similar growth behaviour in the mixing width, since this quantity is predominantly driven by the largest mode of the initial perturbation (inclined interface in both cases).

It should be noted that the mixing width only denotes the large scale feature, i.e. the amplitude of the instability and not the modal content or the scalar mixing. In order to highlight the mixing dynamics, mixed mass materials below the large scale in the flow, and to emphasize the effect of the initial perturbations, mixed-mass $(\mathcal{M})$, mixed-mass thickness for the 2D center slices (δ_{2D}) and three dimensional simulations (δ_{3D}) are defined as

$$\mathcal{M} = \int 4\rho Y_{N_2} Y_{CO_2} dV, \tag{5}$$

$$\delta_{2D} = \frac{\int 4Y_{N_2} Y_{CO_2} dA}{\int dy}, \qquad \delta_{3D} = \frac{\int 4Y_{N_2} Y_{CO_2} dV}{\int dA}, \tag{6}$$

where Y_{N_2} and Y_{CO_2} are the mole fractions of light and heavy gases. Figures 6(b) and 6(c) show the mixed-mass and mixed-mass thickness for both single- and multi-mode initial perturbations, computed from 2D center slices, the entire volume of simulations, and the experimental PLIF images [1, 2]. Before reshock, the multi-mode case has noticeably higher growth rate in both quantities due to the much faster rate of mode merging and mixing. Reshock drastically increases the growth rate and magnitude for both quantities by breaking down the larger scales to much finer scales, and increasing the mixed materials in the flow. However, the growth rate is slightly higher in the single-mode case after reshock due to the stronger shear between two fluids, which generates larger roll-up features at early time after reshock. At later times, this strong Kelvin–Helmholtz instability in the single-mode case enhances the mode merging, and increases the rate of breakdown of large roll-up features to smaller scales. Therefore, there is a larger mixed-mass in the flow compared to the multi-mode case at late time after reshock. While there is a good overall agreement between mixed-mass computed from simulation and experimental PLIF images, the mixed-mass and mixed-mass thickness computed from the simulation at late-time before reshock and early time after reshock is slightly lower in the single-mode case, and slightly higher in the multi-mode case compared to the experimental data.

There are some interesting differences between the mixed-mass thickness computed from 2D center slices and the entire 3D volume. The growth rate and magnitude of these quantities computed from the entire volume is slightly larger than the ones computed from 2D center slices for both single- and multi-mode cases. This indicates that the mixing dynamic and mixed material is not completely uniform along the volume. At early times, the 2D and 3D results are fairly similar, however the difference between them increases as flow evolves in time and the breakdown and merging of coherent structures to smaller scales occur in the flow specially after reshock. As expected, the magnitude of the mixed-mass thickness computed from PLIF images of experimental results are closer to the ones that computed from 2D center slices of the simulation.

C. Circulation

The positive, negative, and total circulation for both single- and multi-mode cases are shown in Fig. 7, which is defined as $\Gamma = \int \omega dA$. Separating out the positive and negative vorticity allows the magnitude of vorticity to be observed, while we can distinguish the dominant vorticity direction before and after reshock interactions. The circulation computed from 2D center slices of simulation is compared to the experimental vorticity measurements obtained from high-speed PIV measurements reported by Carter *et al.* [35] and high resolution data reported by Mohaghar *et al.* [1]. The high-speed PIV data were collected only for the single-mode case, but the high-resolution results were available for both cases. To compare both experimental date set with the simulation with similar resolution and to investigate the grid sensitivity on circulation, this quantity is computed for different grids. The resolution of high-speed PIV data (Figure 7 (a)) is $\approx 4mm/$vector spacing, and it is interesting to note that the circulation computed from this data set is close to the simulation with the lower resolution (grid E). Specifically, the negative circulation at early time after reshock occurs at small scale roll-up features that are not resolved because of the low resolution of high-speed PIV data. The magnitude of both positive and negative circulation is increased by decreasing the grid spacing of simulation (increasing the resolution). The high-resolution experimental data with the resolution of 372 μm/vector spacing (Figures 7 (a) and 7 (b)) is close to the circulation computed from the simulation with the finest grid spacing of 446 μm (grid F) for both single- and multi-mode cases, which is the closest to the experimental PIV resolution [1]. Grid E is not included for the multi-mode case, since the simulation resolution is much lower than the high-resolution PIV experimental results.

Overall, both qualitative and quantitative comparison between experimental and computational results indicate that the simulation is capable of predicting flow behavior with a high level of accuracy. The differences in small scale mixing are largely due to the effect of boundary layer, the higher diffusion thickness, and the higher resolution of PLIF experimental images. The simulation may be improved by modifying the boundary layer, varying the diffusion thickness and increasing the resolution in the future. In addition, the numerical diffusion and dissipation which is effectively setting Reynolds number in the simulations can reduce the fine scale mixing, since the effective numerical viscosity is greater than the physical viscosity in the experiment.

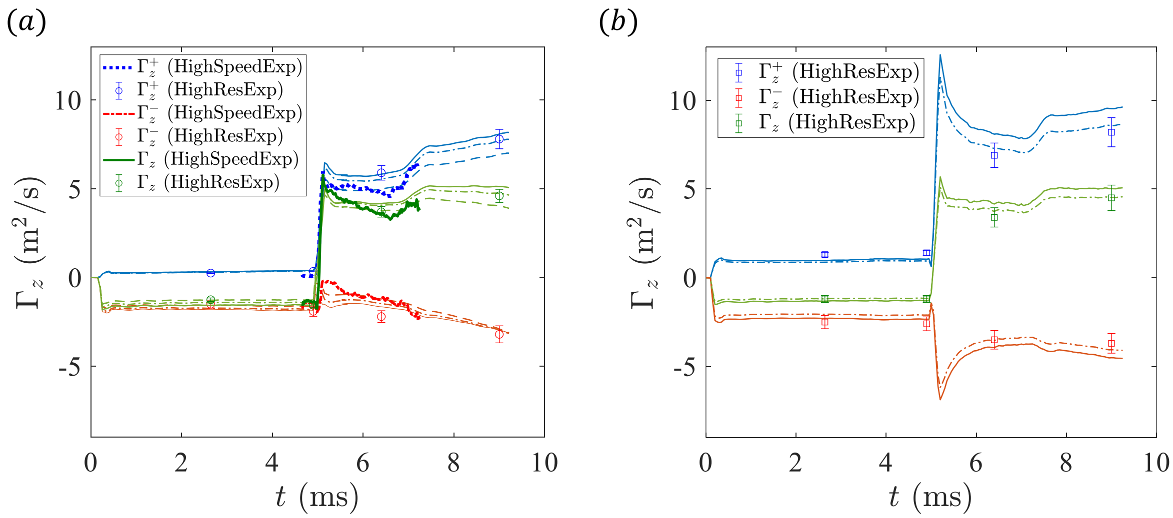

FIG. 7: Comparison of the positive, negative and total circulation between the center slices of 3D simulations computed using different grids and experimental results for (a) single-mode and (b) multi-mode initial perturbations. Simulation: dashed line, grid E; dash-dotted line, grid F; Solid line, grid G. light blue, positive vorticity; light red, negative vorticity, light green, total vorticity.

VI. ANALYSIS OF THREE-DIMENSIONAL SIMULATION RESULTS: THE EFFECTS OF INITIAL PERTURBATIONS

In the previous section, it was shown that the FLASH code, with the defined initial perturbations extracted from the PLIF realizations of experimental results is capable of predicting flow behavior that agrees well with experimental results. The volumetric investigation of shock-driven flow behavior (three-dimensional study) is currently unreliable using experimental techniques due to the effect of large refractive index mismatch at the interface on the laser sheet light. Thus, it is necessary to capitalize on the results from 3D simulations to understand the mixing dynamics in the entire volume. Here, the interaction of the large-wavelength inclined interface with small-scale multi-mode perturbations along the inclined perturbations is studied in the entire volume before and after reshock using 3D simulations. The following section will discuss the development of RMI using predominantly single- and multi-mode initial conditions and provide a qualitative and quantitative comparison that highlights the effects of the multi-mode complex stratified perturbation on top of the base inclined interface.

A. Visualization of the density and vorticity fields

Figure 8 shows the time-evolution of the density iso-surfaces illustrating the dynamics of the bubble and spike at late time before reshock hits the interface (t=5 ms), and at late time after reshock (t=9 ms) for both single- and multi-mode initial perturbations. The iso-surfaces are constructed based on 20 levels that are linearly interpolated values between the data minimum and data maximum of the specific plotted quantity. The shock initially travels from left to right; hence, before reshock, the spikes move from right to left close to the bottom wall, and the bubbles from left to right near the top wall, and after reshock, the overturning motion of the interface reverses the bubble motion from the top to the bottom side, and the spike from the bottom to the top side. For both single- and multi-mode perturbations the largest mode (inclined perturbation) dominates the growth for the entire evolution. However, the mixing mechanism along the inclined perturbations is totally different for the two cases. Before reshock, a range of perturbation length scales grow simultaneously and the flow field consists of a series of mushroom-like structures generated by the deposition of vorticity at the gas interface in the entire volume for the multi-mode case, whereas in the single-mode case, only two to three large modes dominate the growth. After reshock, although the overall mixing is more similar for both cases due to the breakdown of large scales, there are much more fine-scale structures in the entire volume for the multi-mode initial perturbation compared to the single-mode case. This is because the smallest wavelengths were developed before reshock in the mult-mode case, and have had more time to become nonlinear and transition to turbulence. In the single-mode case, the large scale structures start to break down after reshock, but the interface is still coherent and most regions are still connected to each other. On the other hand, in the multi-mode case, the blobs of fluid have separated from the large wavelength perturbation in several regions and there are more evident small scale roll-up features that were merged together and increased mixed material.

Figures 9 and 10 plot a three-dimensional view of different components of the vortices, visualized as iso-surfaces before and after reshock for both initial conditions. Before reshock, similar to density iso-surfaces, the vortex structure in the single-mode interface only includes large scale features along the interface, and the magnitude of streamwise and spanwise components of vorticity is much smaller than the out-of-plane component. Also, the out-of-plane component of vorticity occurs only in the small region of the diffused interface. This is

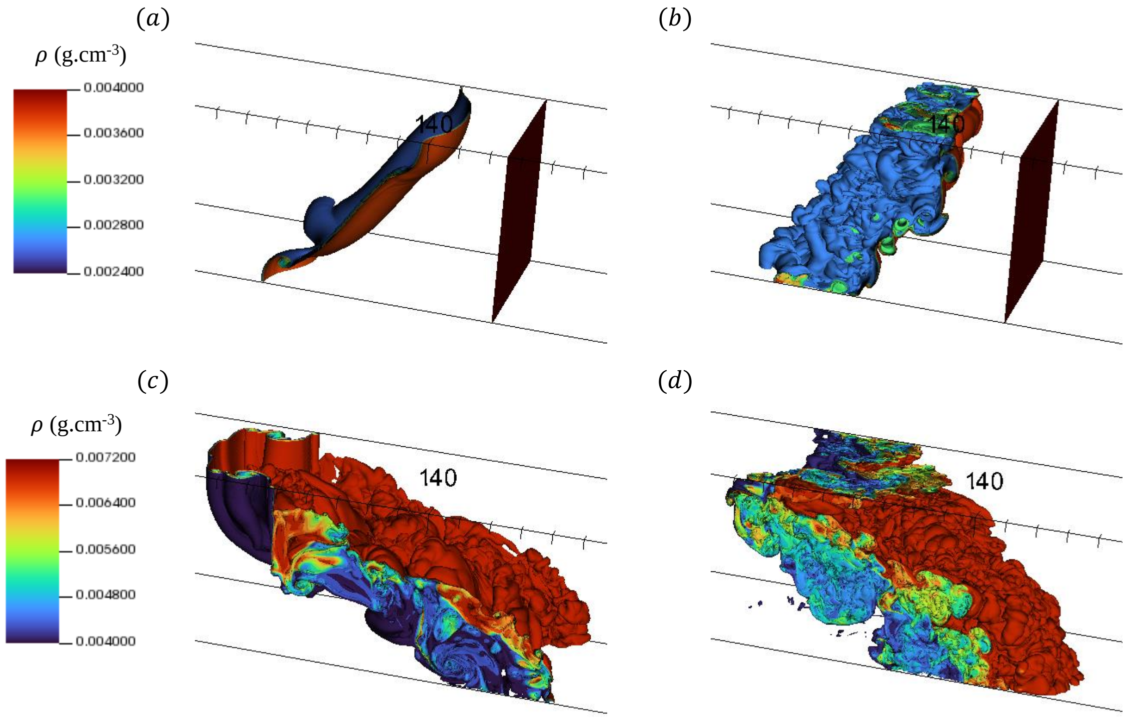

FIG. 8: Iso-surfaces of density corresponding to (a,c) single- and (b,d) multi-mode interfaces (a,c) before (t=5 ms) and (c,d) after (t=9 ms) reshock.

due to the fact that the initial perturbation in the $x-z$ plane was negligible compare to the inclined interface in the $x-y$ plane, which lead to much larger baroclinic vorticity deposition on inclined perturbation. On the other hand, there are several coherent vortex rings at each mushroom shape structure in the multi-mode case. These alternating positive-negative vortices are distributed along the inclined large scale, and the magnitude of streamwise and spanwise components of vorticity is comparable to the out-of-plane component. The out-of-plane component of vorticity is still larger than the other two components, since the dominant mode of the incline wavelength takes a much larger time to be broken down. After reshock, Kelvin–Helmholtz instabilities along the interface grow exponentially and break the coherent vortex rings at late time for both cases. However, the vortex structures are still more coherent in the single-mode case, and they form a larger vortex-tube shape compare to the multi-mode case, where the vortices are concentrated in small worm-like vortex structures typically seen in simulations of turbulent flow fields [37]. The difference between the magnitude of different components of vorticity also decreases as the large scale

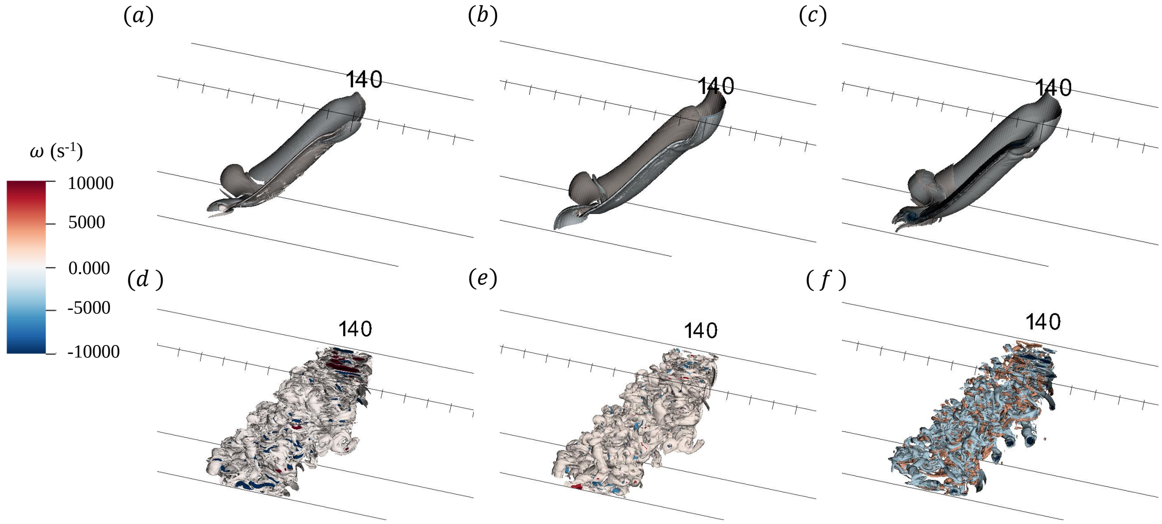

FIG. 9: Iso-surfaces of vorticity in (a,d) x-, (b,e) y- and (c,f) z-direction corresponding to (a,b,c) single- and (d,e,f) multi-mode interfaces before reshock at t=5 ms.

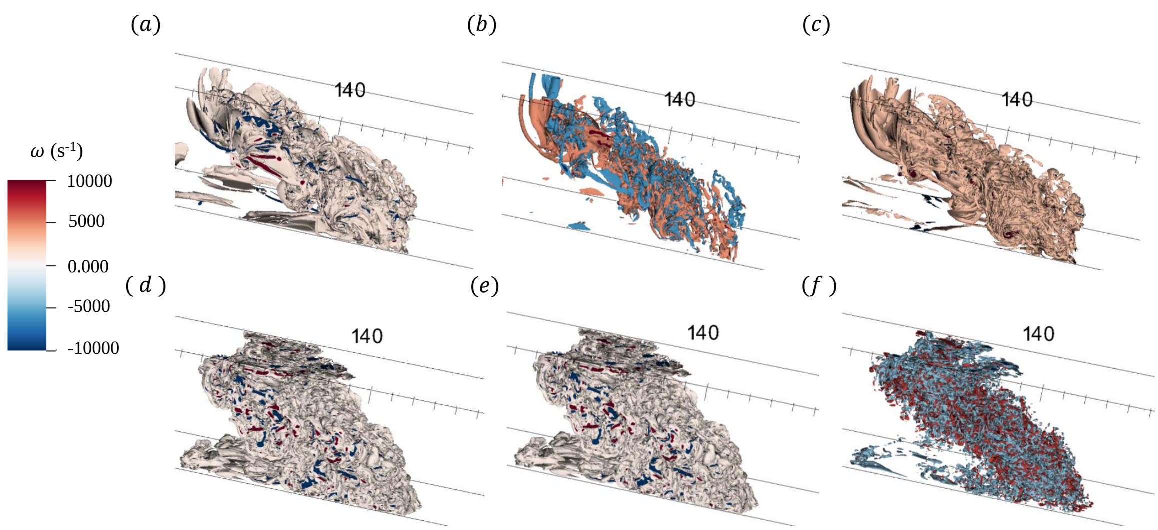

FIG. 10: Iso-surfaces of vorticity in (a,d) x-, (b,e) y- and (c,f) z-direction corresponding to (a,b,c) single- and (d,e,f) multi-mode interfaces after reshock at t=9 ms.

vortices start to break down to smaller structures, which creates mixing in the entire volume.

B. Circulation and baroclinic production

This section provides a quantitative analysis of the evolution of the single- and multi-mode interfaces in three dimensions. The positive, negative and total magnitude of all three components of circulation ($\Gamma = \int \omega dV$) and the volume integral of baroclinic vorticity production ($\mathcal{P} = \nabla\rho \times \nabla p)/\rho^2$) are plotted in Figures 11 and 12. Γ^+, Γ^-, $\mathcal{P}^+$, and $\mathcal{P}^-$ are positive/negative circulation and positive/negative baroclinic production terms, respectively. The evolution of vorticity/circulation and baroclinic vorticity production are analyzed together for better understanding of vorticiy deposition along the interface. Before reshock in the single-mode case, the streamwise component of the circulation is increasing to almost half of the circulation in the spanwise dimension, and the negative circulation in the out-of-plane direction is the most dominant one due to the effect of inclined perturbation in the $x-y$ plane. The small magnitude of streamwise and spanwise components of vorticity is due to the small initial perturbation in the $y-z$ plane for the single-mode case. The baroclinic production in the streamwise dimension also starts at much smaller value compare to spanwise and out-of-plane components, however before reshock hits the interface, and as the initial perturbation grows in the entire volume, the streamwise component of baroclinic production term increases dramatically. This is consistent with the continuous growth in the circulation in the streamwise dimension.

On the other hand for the multi-mode case, the mechanism of vorticity deposition is noticeably different from single-mode case due to the initial small scale multi-mode perturbations on top of the inclined interface. Both positive and negative values of baroclinic vorticity production and circulation in all three dimensions are significantly higher for the multi-mode case. In addition, the spanwise and out-of-plane components of baroclinic vorticity production are almost equal to each other, and the streamwise component quickly (after almost 2.5 ms) rises to the value of spanwise and out-of-plane components of vorticity production. This indicates that the organized initial perturbations in the $x-z$ plane quickly evolve, break down to much finer scales and merge together. This is consistent with the circulation values in all three dimensions. Further, the out-of-plane component of total circulation is dominant similar to the single-mode case due to the presence of inclined large scale. However, unlike the single-mode case, the spanwise component of total circulation in the multi-mode case is a positive value, which is due to the initial perturbations. Compari-

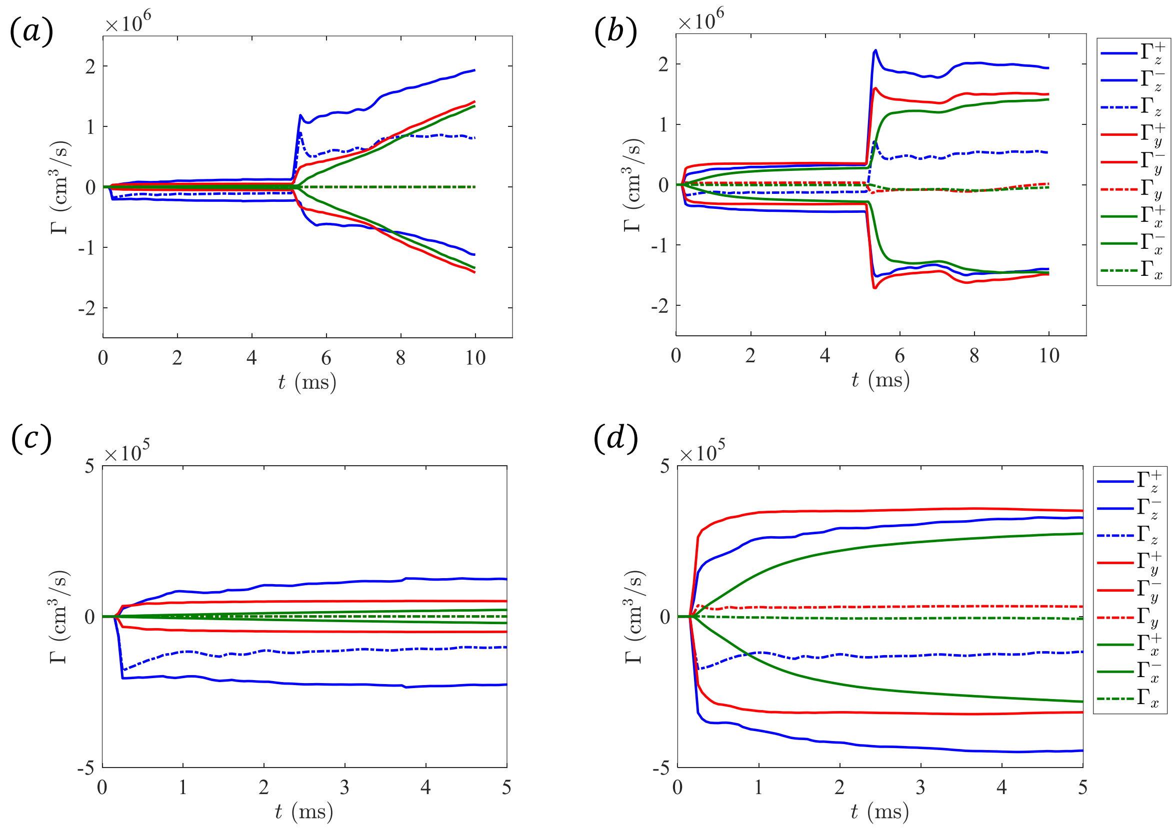

FIG. 11: Evolution of positive, negative and total circulation components for single-mode ((a) before and after reshock, (c) before reshock for clarity) and multi-mode ((b) before and after reshock, (d) before reshock for clarity) initial perturbations.

son of baroclinic production terms between the single- and multi-mode cases indicates that although the inclined large scale is still the dominant scale in the multi-mode flow, the small scale perturbations in the entire flow are rapidly growing and contributing similarly to the total positive and negative production terms.

After reshock, for the single-mode case, the ratio of different components of baroclinic vorticity production and circulation is similar to pre-reshock, where the values of the out-of-plane component is the largest, and the spanwise components of production and circulation are larger than the values in the streamwise dimension. However, reshock causes quick breakdown of large scale vortices in all dimensions of the flow, and there is a sharp increase in both streamwise and spanwise components of production and circulation. At late times after reshock, all three production terms are very similar. For the multi-mode case, similar jump and growth rate in the magnitude of all three components of the baroclinic production

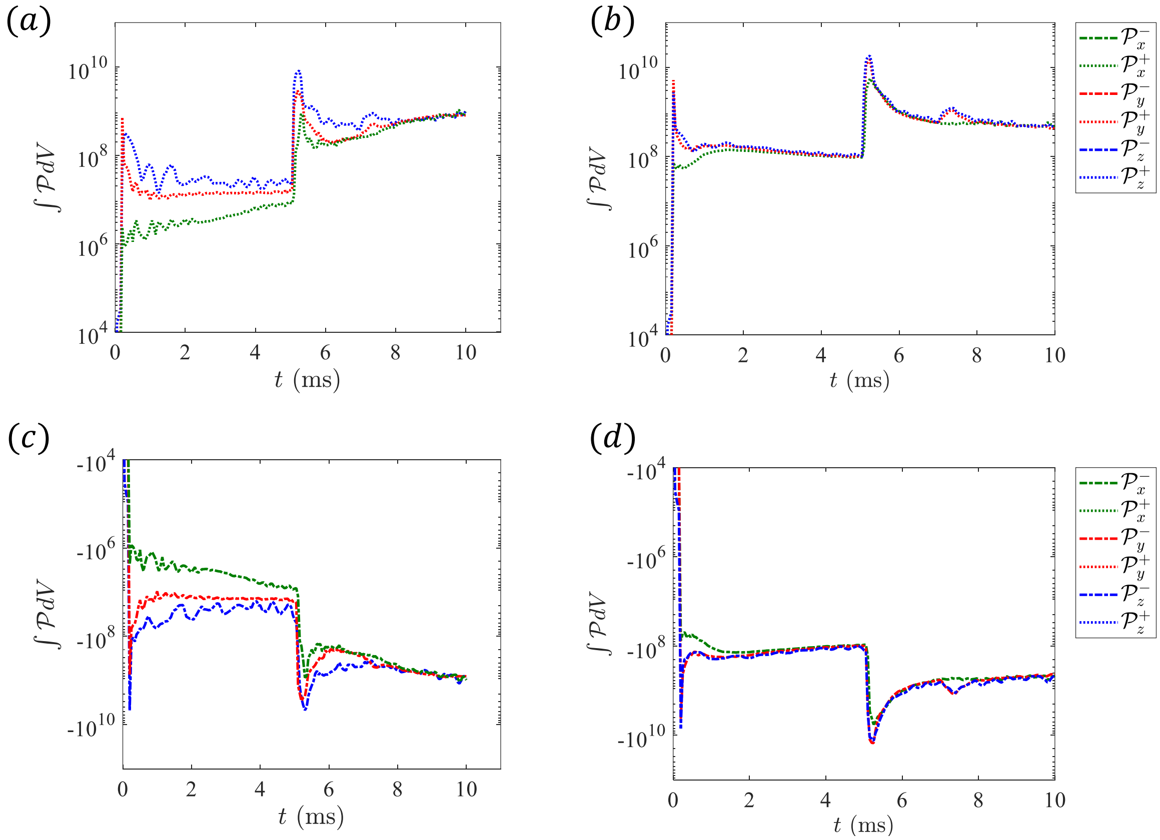

FIG. 12: Evolution of (a,b) positive and (c,d) negative baroclinic production components for (a,c) single-mode and (b,d) multi-mode initial perturbations.

terms are evident due to the fact that the flow is already perturbed in all three dimensions pre-reshock. It should be highlighted that there is not a direct relationship between positive (negative) baroclinic production and positive (negative) circulation. The baroclinic production may be positive (negative) at grid cells with negative (positive) vorticity. However, the positive (negative) baroclinic production term indicate positive (negative) vorticity rate in the flow.

The other interesting observation is the sudden small increase in the magnitude of both negative and positive baroclinic vorticity production and circulation at around 7 to 7.5 ms. A similar jump also was observed in the experimental results [35]. This can be due to the interaction of expansion fans with the interface. These expansion fans are generated when the reshock hits the interface.

C. Density self-correlation

Several turbulence statistics are discussed to have better understanding of the fluctuating components of different variables and turbulence status in the flow. In order to quantify the level of mixing, the average of the density self-correlation in the yz plane (less non-homogenous directions) and in the entire volume is computed using $b = \overline{-(1/\rho)'\rho'}$ [38], and is shown in Fig. 13 and Fig. 14. Although the mixing is obviously not homogeneous along the x-direction, the average in the entire volume along with the understanding of mixing in the inhomogeneous direction (x) can be helpful for the turbulence modeling. The b value of zero corresponds to homogeneously mixed fluid, while large values indicate that there are spatial inhomogeneities in the entire volume. For both initial conditions, b sharply increases after the incident shock wave passes through the interface due to the stretching of the large wavelength. However, the growth rate decreases quickly after around 1-1.5 ms for the multi-mode case because the small scale roll-up features along the interface start to develop and merge together and mix. Thus, although the large scale amplitude of the instability (mixing width) increases similar to the single-mode case, the small scale mixing collapses the growth of the density self-correlation. On the other hand, there is almost uniform growth rate in the single-mode case, since the only mixing along the interface is due to the small diffusion thickness. Also, the b value is slightly higher in the bubble side (positive X), which indicate that more mixing occurs in the spike side.

After reshock, the mixing width and mixed-mass thickness suddenly decrease due to the overturning motion and all mixed materials are located along the spanwise direction, which leads to a sharp decrease in b parameter for both single- and multi-mode cases. As flow evolves in time, and the bubble penetrating to the spike and vice versa, the large wavelength mode develops and the density self correlation increases. However, due to the more mixed materials in the flow after reshock, the growth rate of b collapses quickly for both cases. Moreover, the higher mixed material (slightly lower b value) is on the bubble side due to the overturning motion after reshock. Similar to pre-reshock, the multi-mode case has lower value of b compared to the single-mode case, however the difference decreases because the flow is more mixed in the entire volume for both cases. It should be noted that since the large scale feature is dominant before and after reshock, the flow may need much more time for a complete breakdown of large scales to small scales. Thus, The value of b

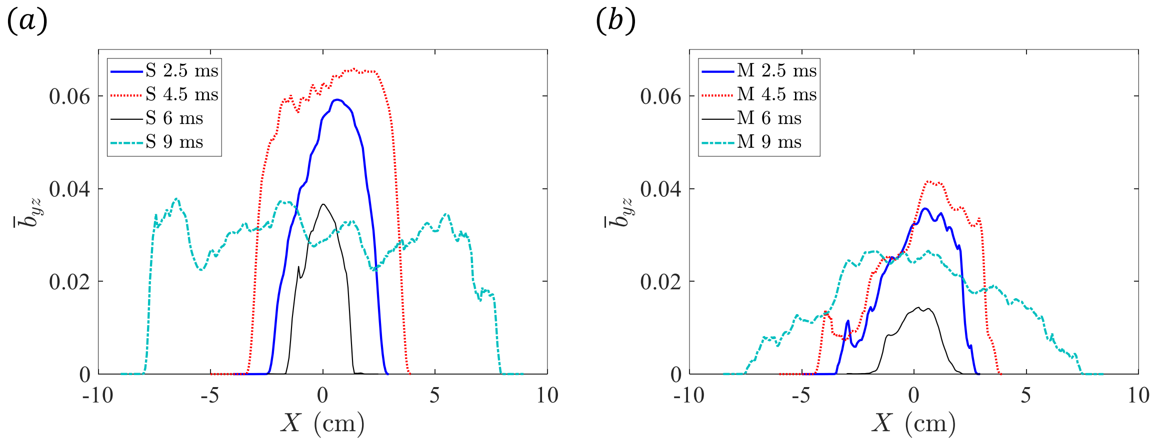

FIG. 13: Profiles of density self-correlation along the streamwise direction before and after reshock for the (a) single-mode and (b) multi-mode initial perturbations. X is the distance from centre of mass.

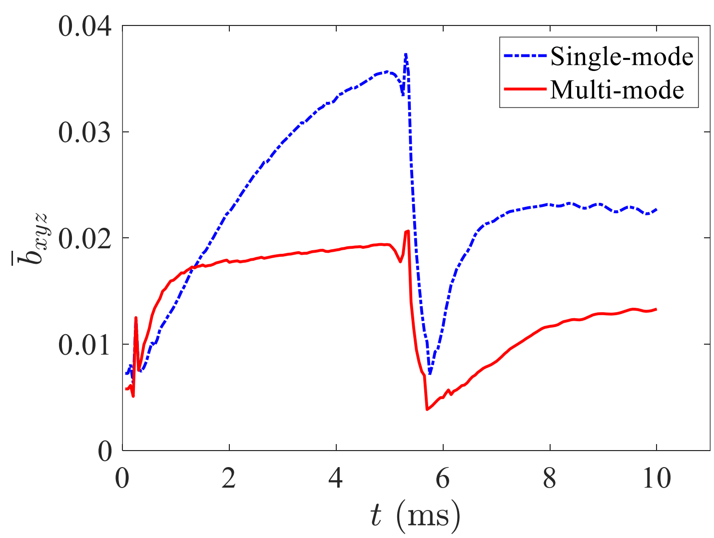

FIG. 14: Evolution of the volume-averaged density self-correlation for single- and multi-mode initial perturbations.

parameter at late non-dimensional times needs further analysis in the future. However, The slow rate of change of density-self-correlation is reported in many previous studies at late non-dimensional times [27, 39, 40].

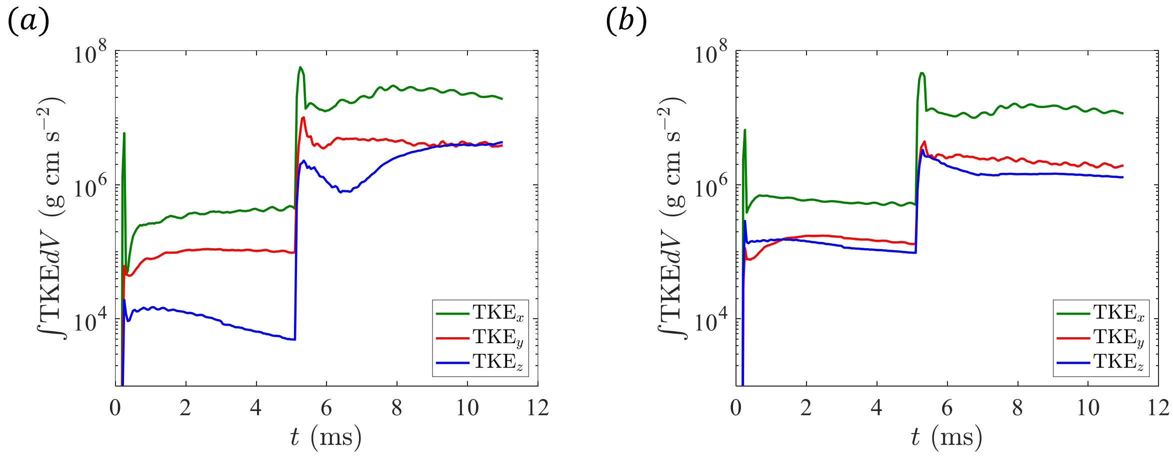

FIG. 15: Evolution of components of turbulent kinetic energy for (a) single- and (b) multi-mode initial perturbations.

D. Turbulent kinetic energy, turbulent mass-flux and anisotropy

The amount of turbulent kinetic energy (TKE) created by incident shock and reshock is shown in Fig. 15. Before and after reshock, the TKE in the streamwise direction is dominant in the flow for the entire evolution for both single- and multi-mode cases due to the effect of the large scale inclined interface, which generates strong shear effects and large relative velocity fluctuation in the streamwise direction (x dimension). However, for the single-mode case before reshock, the TKE in the spanwise direction (y dimension) is much larger than the out-of plane direction (z dimension), while these two quantities are quite similar before and after reshock for the multi-mode case due to the three dimensionality of fluctuations in the multi-mode case. After reshock for the single-mode case, as the larger coherent scales break down quickly in the entire volume, the out-of-plane component of turbulent kinetic energy dramatically increases and the magnitude is similar to the spanwise component at late time. For the multi-mode case, since the scales are already broken down in the entire flow along the interface pre-reshock, reshock is not affecting the ratio of TKE between spanwise and out-of-plane dimensions. Similar to circulation and baroclinic production evolution, after 8 ms, TKE components in the entire volume become very similar to each other, which shows that the flow is much more mixed and the organized, coherent structures in the flow are broken down in all three dimensions. Also, the small jump around 7-7.5 ms is due to the incremental effect of expansion fans on velocity fluctuations.

To have better understanding of the dynamics of velocity fluctuations in the entire flow field, turbulent mass flux ($\overline{\rho}a$) is shown before and after reshock in Fig. 16. The turbulent mass-flux velocity along the streamwise direction is defined as $a_i = \overline{\rho' u_i''}/\overline{\rho}$. The turbulent mass flux is averaged along the spanwise (y) and out-of-plane (z) dimensions (less non-homogenous directions). The turbulent mass flux can explain the findings in the turbulent kinetic energy. Before reshock, the out-of-plane component of a parameter (a_z) is much smaller than the other two components in the single-mode case, while the magnitude of this parameter in the spanwise and out-of-plane directions is similar for the multi-mode case. After reshock in the single-mode case, the magnitude of a in the out-of-plane direction is still smaller than the multi-mode case, however there is a significant increase compare to pre-reshock. For the multi-mode case, there is an alternating positive/negative behavior of mass-flux in the spanwsie and out-of-plane dimensions. This shows that because of perturbed structure of the flow in the $y-z$ plane, the TKE is increasing in one dimension and decreasing in the other dimension, which may be the reason for balanced TKE magnitude in that plane. It should be noted that while turbulent mass flux appears as the primary production term of turbulent kinetic energy for for the Rayleigh-Taylor turbulence or buoyancy-driven homogeneous turbulence due to the background stratification (large mean pressure gradient) [40, 41], it is not necessarily true for the Richtmyer-Meshkov turbulence. Recently, it is shown [42] that the production term related to the turbulent mass flux velocity is not strictly positive, and there is another production term related to the Reynolds stress that is also comparable with the turbulent mass flux velocity term. Thus, due to the complexity of the TKE transport in Richtmyer-Meshkov turbulence, other transport terms such as pressure-strain redistribution, dissipation, etc. should be computed to reach to a certain conclusion for the balanced TKE magnitude .

In addition, the evolution of the volume average of anisotropy tensor is defined as

$$\beta_{ij} = \frac{R_{ij}}{R_{kk}} - \frac{1}{3}\delta_{ij}, \tag{7}$$

where $R_{ij} = \rho u_i'' u_j''$, and δ_{ij} is the Kronecker δ. $\beta = 2/3$ corresponds to having all TKE in the streamwise velocity component, whereas $\beta = -1/3$ corresponds to having no energy in the streamwise component. Figure 17 shows the temporal evolution of $\overline{\beta_{11}}_{xyz}$, which indicates the volume average of TKE contributed from the streamwise component of Reynolds normal stresses. Before reshock, the flow is much more anisotropic in the single-mode case

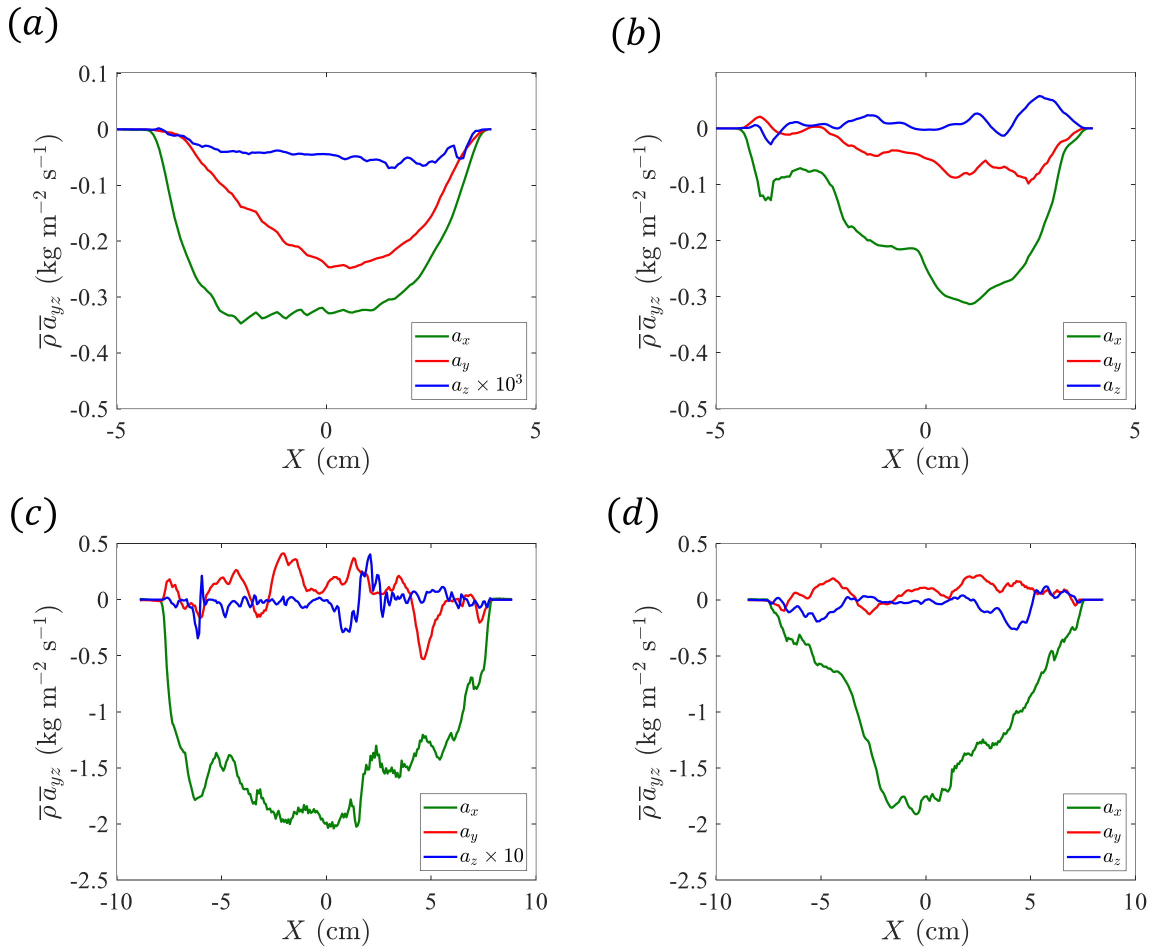

FIG. 16: Profiles of turbulent mass-flux components in the streamwise direction (a,b) before (t=5 ms) and (c,d) after reshock (t=9 ms) for the (a,c) single-mode and (b,d) multi-mode initial perturbations. X is the distance from centre of mass.

compare to the multi-mode case. The anisotropy increases with time since the large scale inclined interface stretches and the shear effect generates large relative velocity fluctuation, i.e. significant increase in the streamwise component of TKE.

After reshock, the volume average of anisotropy is almost equal for both cases and the flow moves toward isotropy at early time due to the overturning motion and the sudden decrease in the large scale amplitude. As the interface stretches again in the steamwise direction, the anisotropy slightly increases, however It is interesting to note that the small scale mixing in the entire volume collapses the growth rate of anisotropy quickly and $\overline{\beta_{11}}_{xyz}$ reaches to a similar asymptotic value for both cases. Running simulations to much later times are required to discuss about the anisotropy in such flows with large anisotropy at

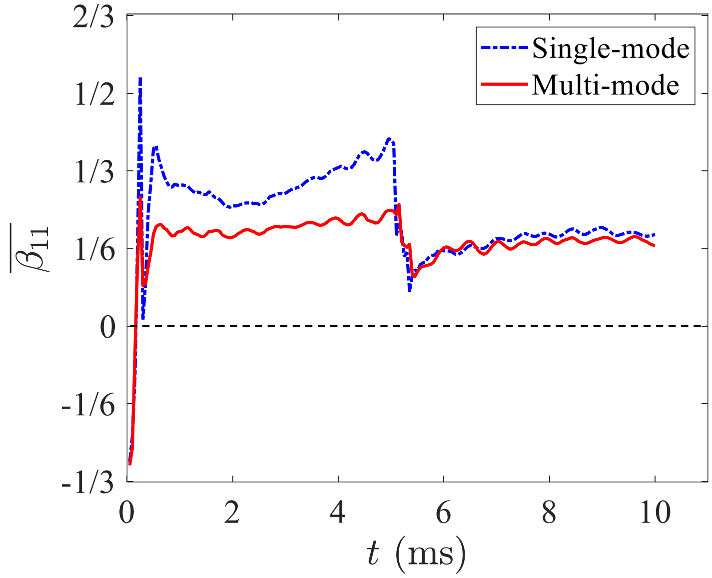

FIG. 17: Evolution of the volume-averaged anisotropy for single- and multi-mode initial perturbations.

late non-dimensional times, which can be performed in future works.

VII. CONCLUSIONS

The volumetric investigation of Richtmyer-Meshkov instability using the current experimental techniques can incorporate large errors due to refractive index mismatch at the interface. Thus, it is necessary to take advantage of the computational capabilities to understand the flow behavior and mixing dynamics in the entire volume during RM evolution. This study has extended the previous computational work of McFarland *et al.* [3] by investigating the effects of small scale multi-mode initial perturbations on top of predominantly single-mode inclined interface during the evolution of mixing layer induced by Richtmyer–Meshkov instability through carefully designed three-dimensional simulations using FLASH code. The initial perturbations of both single- and multi-mode cases are precisely defined based on the experimental PLIF images of Mohaghar *et al.* [1], and the entire experimental shock tube domain is used for the simulation setup. To verify the capability of the code to predict flow behavior accurately, mixing width, mixed-mass, mixed-mass thickness and circulation computed from two-dimensional center slices of 3D simulations are compared with the experimental results [1, 29, 35]. The qualitative and quantitative analyses indicate that the results from simulations are in a reasonably good agreement with the experimental results. The three-dimensional simulations lead to a number of major conclusions. Although the long wavelength inclined interface dominates the flow motion for both single- and multi-mode cases before and after reshock, the short-wavelength multi-mode perturbations along the inclined interface produce completely different mixing mechanism compare to the single-mode case.

Before reshock, the initial coherent small scale perturbations quickly break down into still smaller structures along the interface. At later time, the roll-up features start to merge together and coherent vortex structures break down into smaller vortex-tube formations. Comparison between mixed-mass and mixed-mass thickness computed from 2D center slices and the entire volume indicates that the mixing is not uniform in different regions of the multi-mode case. Due to the small scale perturbations, barocline vorticity production and circulation (vorticity deposition) is much larger in the multi-mode case, and different components of circulation are comparable, which is another indication of three-dimensionality of the mixed materials and vortex structures. Due to the merging of roll-up features in the entire volume, the growth rate of density self-correlation sharply decreases at later times before reshock in the multi-mode case. Although the streamwise component of turbulent kinetic energy and turbulent mass flux is larger than the other two components for both cases due to the large shear effect of large wavelength inclined interface, the spanwise and out-of-plane components of these quantities are much larger in the multi-mode case, which indicates fluctuations occur in the entire volume. Because of these larger fluctuations, the anisotropy is significantly smaller in the flow for the multi-mode case.

After reshock, larger coherent scales of the flow quickly break down to much finer disorganized scales due to the additional deposited vorticity by reshock that is more than two orders of magnitude larger than that of the initial vorticity deposition. Although there are noticeable differences between the flow morphology of the single- and multi-mode cases, reshock eliminates most of the memory of the initial interface perturbations. The similarity between mixed-mass and mixed-mass thickness of 2D center slices and 3D volume exhibits that the mixed material is distributed in the entire volume. At early time after reshock, the baroclinic vorticity production and circulation are much larger in the multi-mode case due to the vorticity deposited on the pre-reshock perturbed interface. However, all three components of both quantities grow much faster in the single-mode case, and the magnitudes are similar for both cases at late time after reshock. The out-of plane component of turbulent kinetic energy and turbulent mass flux in the single-mode case also rises quickly to a value comparable to the spanwise component. Thus, the three-dimensionality of mixing and fluctuations is apparent for both cases at late time after reshock. The volume-averaged anisotropy is also similar during the temporal evolution after reshock for both cases. The flow moves toward isotropy due to the overturning motion at early time after reshock, while the stretching of the interface increases the magnitude to an asymptotic value, which is much smaller than pre-reshock due to the large fluctuations in all three-dimensions.

ACKNOWLEDGMENTS

This work was supported by the National Science Foundation Faculty Early Career Development (CAREER) Award (award no. 1451994). This research was supported in part through research cyberinfrastructure resources and services provided by the Partnership for an Advanced Computing Environment (PACE) at the Georgia Institute of Technology, Atlanta, Georgia, USA. The software used in this work was developed in part by the DOE NNSA ASC- and DOE Office of Science ASCR-supported Flash Center for Computational Science at the University of Chicago.

[1] M. Mohaghar, J. Carter, B. Musci, D. Reilly, J. McFarland, and D. Ranjan, Evaluation of turbulent mixing transition in a shock-driven variable-density flow, J. Fluid Mech. **831**, 779 (2017).

[2] M. Mohaghar, J. Carter, G. Pathikonda, and D. Ranjan, The transition to turbulence in shock-driven mixing: Effects of Mach number and initial conditions, Journal of Fluid Mechanics **871**, 595 (2019).

[3] J. A. McFarland, D. Reilly, W. Black, J. A. Greenough, and D. Ranjan, Modal interactions between a large-wavelength inclined interface and small-wavelength multimode perturbations in a Richtmyer–Meshkov instability, Phys. Rev. E **92**, 013023 (2015).

[4] R. D. Richtmyer, Taylor instability in shock acceleration of compressible fluids, Commun. Pure Appl. Maths **13**, 297 (1960).

[5] E. E. Meshkov, Instability of the interface of two gases accelerated by a shock wave, Fluid Dyn. **4**, 101 (1969).

[6] M. Brouillette, The Richtmyer–Meshkov instability, Annu. Rev. Fluid Mech. **34**, 445 (2002).

[7] D. Ranjan, J. Oakley, and R. Bonazza, Shock-bubble interactions, Annu. Rev. Fluid Mech. **43**, 117 (2011).

[8] Y. Zhou, Rayleigh–Taylor and Richtmyer-Meshkov instability induced flow, turbulence, and mixing. I, Phys. Reports **720**, 1 (2017).

[9] Y. Zhou, Rayleigh–Taylor and Richtmyer-Meshkov instability induced flow, turbulence, and mixing. II, Phys. Reports **723**, 1 (2017).

[10] J. D. Lindl, O. Landen, J. Edwards, E. d. Moses, N. Team, *et al.*, Review of the National Ignition Campaign 2009-2012, Phys. Plasmas **21**, 020501 (2014).

[11] D. Arnett, The role of mixing in astrophysics, The Astrophysical Journal Supplement Series **127**, 213 (2000).

[12] F. E. Marble, G. J. Hendricks, and E. E. Zukoski, Progress toward shock enhancement of supersonic combustion processes, in *Turbulent Reactive Flows* (Springer, 1989) pp. 932–950.

[13] O. Schilling and M. Latini, High-order WENO simulations of three-dimensional reshocked Richtmyer–Meshkov instability to late times: dynamics, dependence on initial conditions, and comparisons to experimental data, Acta Math. Scientia **30**, 595 (2010).

[14] D. Reilly, J. McFarland, M. Mohaghar, and D. Ranjan, The effects of initial conditions and circulation deposition on the inclined-interface reshocked Richtmyer–Meshkov instability, Exp. Fluids **56**, 1 (2015).

[15] B. J. Balakumar, G. C. Orlicz, C. D. Tomkins, and K. P. Prestridge, Dependence of growth patterns and mixing width on initial conditions in Richtmyer–Meshkov unstable fluid layers, Phys. Scr. **2008**, 014013 (2008).

[16] S. Balasubramanian, G. C. Orlicz, K. P. Prestridge, and B. J. Balakumar, Experimental study of initial condition dependence on Richtmyer–Meshkov instability in the presence of reshock, Phys. Fluids **24**, 034103 (2012).

[17] C. R. Weber, N. Haehn, J. Oakley, D. Rothamer, and R. Bonazza, Turbulent mixing measurements in the Richtmyer–Meshkov instability, Phys. Fluids **24**, 074105 (2012).

[18] C. R. Weber, N. S. Haehn, J. G. Oakley, D. A. Rothamer, and R. Bonazza, An experimental investigation of the turbulent mixing transition in the Richtmyer–Meshkov instability, J. Fluid Mech. **748**, 457 (2014).

[19] M. M. Mansoor, S. M. Dalton, A. A. Martinez, T. Desjardins, J. J. Charonko, and K. P. Prestridge, The effect of initial conditions on mixing transition of the Richtmyer–Meshkov instability, Journal of Fluid Mechanics **904** (2020).

[20] B. Thornber, D. Drikakis, D. L. Youngs, and R. J. R. Williams, The influence of initial conditions on turbulent mixing due to Richtmyer–Meshkov instability, Journal of Fluid Mechanics **654**, 99 (2010).

[21] M. Groom and B. Thornber, The influence of initial perturbation power spectra on the growth of a turbulent mixing layer induced by Richtmyer–Meshkov instability, Physica D: Nonlinear Phenomena **407**, 132463 (2020).

[22] D. J. Hill, C. Pantano, and D. I. Pullin, Large-eddy simulation and multiscale modelling of a Richtmyer–Meshkov instability with reshock, J. Fluid Mech. **557**, 29 (2006).

[23] M. Latini, O. Schilling, and W. Don, Effects of WENO flux reconstruction order and spatial resolution on reshocked two-dimensional Richtmyer–Meshkov instability, J. Comput. Phys. **221**, 805 (2007).

[24] J. T. Morán-López and O. Schilling, Multicomponent Reynolds-averaged Navier–Stokes simulations of reshocked Richtmyer–Meshkov instability-induced mixing, High Energy Density Physics **9**, 112 (2013).

[25] M. Lombardini, D. Hill, D. Pullin, and D. Meiron, Atwood ratio dependence of richtmyer–meshkov flows under reshock conditions using large-eddy simulations, Journal of fluid mechanics **670**, 439 (2011).

[26] M. Lombardini, D. I. Pullin, and D. I. Meiron, Transition to turbulence in shock-driven mixing: a Mach number study, J. Fluid Mech. **690**, 203 (2012).

[27] V. K. Tritschler, B. J. Olson, S. K. Lele, S. Hickel, X. Y. Hu, and N. A. Adams, On the Richtmyer–Meshkov instability evolving from a deterministic multimode planar interface, J. Fluid Mech. **755**, 429 (2014).

[28] M. L. Wong, D. Livescu, and S. K. Lele, High-resolution Navier-Stokes simulations of Richtmyer-Meshkov instability with reshock, Physical Review Fluids **4**, 104609 (2019).

[29] M. Mohaghar, *Effects of initial conditions and Mach number on turbulent mixing transition of shock-driven variable-density flow*, Ph.D. thesis, Georgia Institute of Technology (2019).

[30] J. A. McFarland, J. A. Greenough, and D. Ranjan, Computational parametric study of a Richtmyer–Meshkov instability for an inclined interface, Phys. Rev. E **84**, 026303 (2011).

[31] B. Fryxell, K. Olson, P. Ricker, F. X. Timmes, M. Zingale, D. Q. Lamb, P. MacNeice, R. Rosner, J. W. Truran, and H. Tufo, FLASH: An adaptive mesh hydrodynamics code for modeling astrophysical thermonuclear flashes, The Astrophysical Journal Supplement Series **131**, 273 (2000).

[32] A. C. Calder, B. C. Curts, L. J. Dursi, B. Fryxell, G. Henry, P. MacNece, K. Olson, P. Ricker, R. Rosner, F. X. Timmes, H. M. Tufo, J. W. Truran, and M. Zingale, High-performance reactive fluid flow simulations using adaptive mesh refinement on thousands of processors, in *SC'00: Proceedings of the 2000 ACM/IEEE Conference on Supercomputing* (IEEE, 2000) pp. 56–56.

[33] J. Dahal and J. A. McFarland, A numerical method for shock driven multiphase flow with evaporating particles, Journal of Computational Physics **344**, 210 (2017).

[34] N. Attal and P. Ramaprabhu, Numerical investigation of a single-mode chemically reacting Richtmyer-Meshkov instability, Shock Waves **25**, 307 (2015).

[35] J. Carter, G. Pathikonda, N. Jiang, J. J. Felver, S. Roy, and D. Ranjan, Time-resolved measurements of turbulent mixing in shock-driven variable-density flows, Scientific reports **9**, 1 (2019).

[36] D. H. Olson and J. W. Jacobs, Experimental study of Rayleigh–Taylor instability with a

complex initial perturbation, Phys. Fluids **21**, 034103 (2009).

[37] B. Thornber, D. Drikakis, and D. Youngs, Large-eddy simulation of multi-component compressible turbulent flows using high resolution methods, Computers & fluids **37**, 867 (2008).

[38] D. Besnard, F. H. Harlow, R. M. Rauenzahn, and C. Zemach, *Turbulence transport equations for variable-density turbulence and their relationship to two-field models*, Tech. Rep. (Los Alamos National Lab., lA-12303-MS, 1992).

[39] S. Balasubramanian, G. C. Orlicz, and K. P. Prestridge, Experimental study of initial condition dependence on turbulent mixing in shock-accelerated Richtmyer–Meshkov fluid layers, Journal of Turbulence **14**, 170 (2013).

[40] C. D. Tomkins, B. J. Balakumar, G. Orlicz, K. P. Prestridge, and J. R. Ristorcelli, Evolution of the density self-correlation in developing Richtmyer–Meshkov turbulence, J. Fluid Mech. **735**, 288 (2013).

[41] D. Livescu and J. R. Ristorcelli, Variable-density mixing in buoyancy-driven turbulence, J. Fluid Mech. **605**, 145 (2008).

[42] M. L. Wong, J. R. Baltzer, D. Livescu, and S. K. Lele, Analysis of second moments and their budgets for Richtmyer-Meshkov instability and variable-density turbulence induced by reshock, Physical Review Fluids **7**, 044602 (2022).